JJMIE

Volume 1, Number 1, Sep. 2007
ISSN 1995-6665
Pages 31 - 41

Jordan Journal of Mechanical and Industrial Engineering

A Nonlinear Torsional Dynamic Model of Multi-Mesh Gear Trains Having Flexible Shafts

Ahmad Al-Shhyab [a,*], Ahmet Kahraman [b]

[a] *Department of Mechanical Engineering, Hashemite University, P.O. Box 330127, Zarqa 13133, Jordon*
[b] *Department of Mechanical Engineering, The Ohio State University, 650 Ackerman Road, Columbus, OH 43202, USA*

Abstract

A non-linear time-varying dynamic model is developed to study torsional dynamic behavior of a typical multi-mesh gear train. The physical system consists of M shafts ($M \geq 2$) coupled to each other by $M-1$ gear pairs. The discrete dynamic model includes the gear backlash clearance, gear mesh stiffness fluctuations, and torsional flexibilities of the shafts. In addition, the gear tooth modifications and typical manufacturing errors are included in the form of periodically time-varying displacement functions applied at gear meshes. A multi-term Harmonic Balance formulation is used in conjunction with discrete Fourier Transforms and a Parametric Continuation technique to obtain the steady-state period-n motions. Direct numerical integration results are used to demonstrate the accuracy of the harmonic balance predictions. Effects of key system parameters are also studied.

Keywords: Gear ;HBM; Multi-mesh; Time-varying; Discrete Fourier; Torsional;

Nomenclature

List of Symbols:

b	half length of backlash
c	damping coefficient
e	gear transmission error
f	external force
g	discontinuous displacement function
HBM	Harmonic Balance Method
I	polar mass moment of inertia
J	Jacobian matrix
k	gear mesh stiffness
M	Monodromy matrix
m	mass, frequency multiplier
p	relative gear mesh displacement
Q	number of discrete time points
q	discrete time interval
R	number of harmonic components considered in the solution
r	base radius
S	matrix form of non-linear algebraic equation set
T	torque
t	time
u	displacement harmonic amplitude
U	displacement vector
Z	number of gear teeth
δ	kronecker delta
Λ	dimensionless frequency
κ	dimensionless mesh stiffness
θ	rotational displacement
ω	frequency
Ω	nominal angular velocity
ζ	damping ratio

Subscripts:

c	characteristic quantity
eq	equivalent
i	gear or shaft index
i,n	natural mode I
m	mesh
s	shaft

Superscripts:

rms	root-mean-square value
T	matrix transpose

* Corresponding author. e-mail: alshyyab@hu.edu.jo

1. Introduction

Gear system dynamics has been a major research topic for the last two decades since both fatigue life and noise behavior of a gear set are impacted by its dynamic behavior. The dynamic response of the gear system shown in Figure 1 will be studied in this paper. The system is formed by M parallel shafts, coupled to each other by $M-1$ gear meshes formed by $2M-2$ gears. Input and output shafts are connected to rigid inertias representing prime mover (input) and output inertias, respectively. This configuration can be found in a wide range of automotive (manual, automatic and continuously variable transmissions), aerospace (rotorcraft drive trains), marine, wind turbine and industrial applications.

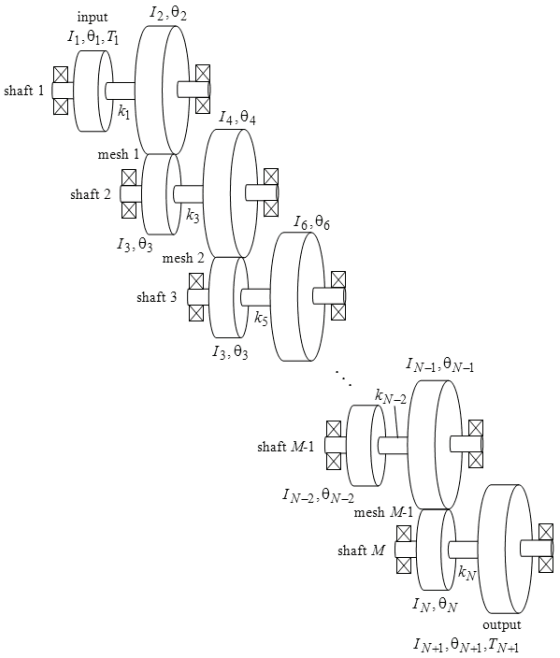

Figure 1: An M-shaft gear train configuration considered in this study

A number of dynamic models were proposed in the past to describe the dynamic behavior of multi-shaft gear system. Most of these models were linear time-invariant type as the gear backlash and mesh stiffness fluctuations were both ignored [1-10]. Such simplifications allowed a larger number of degrees of freedom to be included in the models since Eigen Value and Modal Summation formulations were suitable. Shaft and bearing flexibilities and combined transverse-torsional motions of gears were all included in these models to study larger scale gear-shaft-bearing systems. In some cases, the case deflections were also included in the form of a case stiffness matrix [10]. While these models offered guidelines towards the design of gear systems with favorable shaft and bearing arrangements, they brought limited insight to the behavior at the gear mesh. Another group of models [11-14] included the mesh stiffness fluctuations in the form of a parametric excitation while still assuming no tooth separations. These studies focused on the instabilities caused by parametric excitations and predicted primary and parametric resonances, resulting in regions of unstable motions with infinitely large amplitudes. These models as well were not capable of describing the non-linear behavior observed in recent experimental data [9,15-18] due to backlash-induced tooth separations.

Models of Kahraman and Blankenship [16,17] included both the gear backlash and mesh stiffness fluctuations on a single spur gear pair, and exhibited a softening type nonlinear behavior for a single gear pair due to apparent tooth separations. They also demonstrated that their single gear pair model correlates well with experimental data. Most recently, these authors [19,20] proposed a nonlinear time-varying dynamic model of the system shown in Figure 1 for a case of three shafts and two gear pairs. The system was reduced to a two degree of freedom definite model by using the relative gear mesh displacements as the coordinates and assuming rigid shafts. Dimensionless equations of motion were solved for the steady state period-1 motions [19] and period-n sub-harmonic motions [20] by using a multi-term Harmonic Balance method (HBM) in conjunction with discrete Fourier transforms and a parametric continuation scheme. These solutions were shown to compare well with the direct numerical integration solutions. Floquet theory was applied to determine the stability of the steady state solutions. An example gear train was used to investigate the influence of key system parameters including alternating mesh stiffness amplitudes, gear mesh damping, and torque transmitted.

These earlier models [19,20] were limited in several aspects: (i) they considered only a 3-shaft, 2-gear pair configuration, (ii) the torsional flexibilities of the shafts were not included in the model resulting in same vibration amplitudes for two gears mounted on the same shaft, and (iii) the input and output inertias were not included. This paper aims at generalizing these previous models [19,20] by considering any number of shafts, and including both the torsional shaft flexibilities and input/output inertias. The model will include $N+1$ inertia elements ($N+1$ degrees of freedom) where $N=2M-1$, with I_1 and I_{N+1} representing input and output inertias, respectively. The multi-term HBM that was used successfully for the three-shaft system [19,20] will be extended here as well as for the steady state periodic solutions of this M-shaft system including both period-1 and period-n sub-harmonic motions.

2. Dynamic Model Formulation

A dynamic model of a segment of the M-shaft gear train of in Figure 1 is shown in Figure 2. Equations of motion of the overall system are given as:

$$I_1\ddot{\theta}_1(\bar{t}) + c_1\dot{\bar{p}}_1(\bar{t}) + k_1\bar{p}_1(\bar{t}) = T_1(\bar{t}) \qquad (1a)$$

$$I_2\ddot{\theta}_2(\bar{t}) - c_1\dot{\bar{p}}_1(\bar{t}) - k_1\bar{p}_1(\bar{t}) + r_2c_2\dot{\bar{p}}_2(\bar{t}) + r_2k_2(\bar{t})\bar{g}_2(\bar{t}) = 0 \qquad (1b)$$

$$\vdots$$

$$I_N\ddot{\theta}_N(\bar{t}) + c_N\dot{\bar{p}}_N(\bar{t}) + k_N\bar{p}_N(\bar{t}) + r_Nc_{N-1)}\dot{\bar{p}}_{(N-1)}(\bar{t}) + r_{(N-1)}k_{(N-1)}(\bar{t})\bar{g}_{(N-1)}(\bar{t}) = 0 \qquad (1c)$$

$$I_{N+1}\ddot{\theta}_{N+1}(\bar{t}) - c_N\dot{\bar{p}}_N(\bar{t}) - k_N\bar{p}_N(\bar{t}) = T_{N+1}(\bar{t}) \qquad (1d)$$

where $N = 2M - 1$, an overdot denotes differentiation with respect to time $\bar{t}$, and

$$\bar{p}_n(\bar{t}) = \begin{cases} \theta_n(\bar{t}) - \theta_{n+1}(\bar{t}), & n = odd, \\ r_n\theta_n(\bar{t}) + r_{n+1}\theta_{n+1}(\bar{t}) + \bar{e}_n(\bar{t}), & n = even. \end{cases} \quad (2)$$

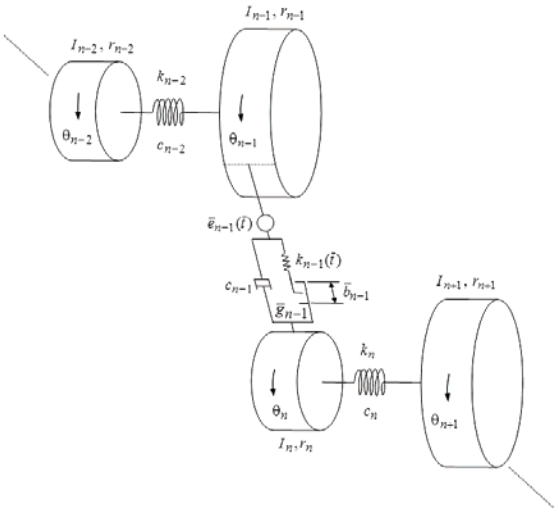

Figure 2: Torsional dynamic model of a segment of the the gear train shown in Figure 1

Here, $\bar{p}_n(\bar{t})$ with $n = odd$ represents torsional shaft deflections between two gears (or a gear and a rigid disk) and $\bar{p}_n(\bar{t})$ with $n = even$ represents relative displacements at a gear mesh formed by gear inertias n and $n+1$ along the line of action. r_n and r_{n+1} are the base circle radii of the gear pair formed by gears n and $n+1$. Torsional shaft flexibilities are represented by the torsional stiffness and damping coefficients, k_n and c_n ($n = odd$) as shown in Figure 2. The flexibility of a gear mesh is modeled by a periodically time-varying mesh stiffness $k_n(\bar{t})$ ($n = even$) that is subjected to a nonlinear displacement function $\bar{g}_n(\bar{t})$ representing the gear backlash clearance

$$\bar{g}_n(\bar{t}) = \begin{cases} \bar{p}_n(\bar{t}) - \bar{b}_n, & \bar{p}_n(\bar{t}) > \bar{b}_n \\ 0, & |\bar{p}_n(\bar{t})| \le \bar{b}_n \\ \bar{p}_n(\bar{t}) + \bar{b}_n, & \bar{p}_n(\bar{t}) < -\bar{b}_n \end{cases}, \quad n = even. \quad (3)$$

In addition, c_n and $2\bar{b}_n$ are the gear mesh damping coefficient and amount of backlash at the gear mesh n (formed by gear inertias n and $n+1$, $n = even$), respectively. Finally, $\bar{e}_n(\bar{t})$ in Figure 2 and equation (2) represents the so-called static transmission error excitation at the mesh of gears n and $n+1$ that accounts for intentional gear tooth profile modifications and manufacturing errors.

The system shown in Figure 2 is semi-definite with a zero-valued natural frequency. This rigid body mode can be eliminated by using $\bar{p}_n(\bar{t})$ as the coordinates. Also defining a characteristic length b_c and a characteristic frequency ω_c such that

$$p_n(\bar{t}) = \begin{cases} \bar{p}_n(\bar{t}), & n: odd, \\ \bar{p}_n(\bar{t})/b_c, & n: even, \end{cases} \qquad e_n(\bar{t}) = \bar{e}_n(\bar{t})/b_c \quad (4a,b)$$

and a dimensionless time $t = \omega_c\bar{t}$, dimensionless form of equations (1) can be written as

$$\ddot{p}_1(t) + 2\zeta_{11}\omega_{11}\dot{p}_1(t) - 2\zeta_{12}\omega_{12}\dot{p}_2(t) + \omega_{11}^2 p_1(t) - \omega_{12}^2\kappa_2(t)g_2(t) = f_1(t) \quad (5a)$$

$$\ddot{p}_2(t) - 2\zeta_{21}\omega_{21}\dot{p}_1(t) + 2\zeta_{22}\omega_{22}\dot{p}_2(t) + 2\zeta_{23}\omega_{23}\dot{p}_3(t) - \omega_{21}^2 p_1(t) + \omega_{22}^2\kappa_2(t)g_2(t) + \omega_{23}^2 p_3(t) = \ddot{e}_2(t) \quad (5b)$$

$$\ddot{p}_n + 2\zeta_{n(n-1)}\omega_{n(n-1)}\dot{p}_{(n-1)} + 2\zeta_{nn}\omega_{nn}\dot{p}_n - 2\zeta_{n(n+1)}\omega_{(n)(n+1)}\dot{p}_{(n+1)} + \omega_{n(n-1)}^2\kappa_{(n-1)}(t)g_{(n-1)} + \omega_{nn}^2 p_n - \omega_{n(n+1)}^2\kappa_{(n+1)}(t)g_{(n+1)} = 0, \quad n = 3,5,\cdots,N-3 \quad (5c)$$

$$\ddot{p}_n - 2\zeta_{n(n-1)}\omega_{n(n-1)}\dot{p}_{(n-1)} + 2\zeta_{nn}\omega_{nn}\dot{p}_n + 2\zeta_{n(n+1)}\omega_{n(n+1)}\dot{p}_{(n+1)} - \omega_{n(n-1)}^2 p_{(n-1)} + \omega_{nn}^2\kappa_n(t)g_n + \omega_{n(2n+1)}^2 p_{(n+1)} = \ddot{e}_n(t), \quad n = 4,6,\ldots,N-2 \quad (5d)$$

$$\ddot{p}_N(t) + 2\zeta_{N(N-1)}\omega_{N(N-1)}\dot{p}_{(N-1)}(t) + 2\zeta_{NN}\omega_{NN}\dot{p}_N(t) + \omega_{N(N-1)}^2\kappa_{(N-1)}(t)g_{(N-1)}(t) + \omega_{NN}^2 p_N(t) = f_N(t). \quad (5e)$$

Here, dimensionless mesh stiffness functions are defined as $\kappa_n(\bar{t}) = 1 + \hat{k}_n(\bar{t})/\bar{k}_n$ ($n = even$) where $\bar{k}_n$ and $\hat{k}_n(\bar{t})$ are the mean and alternating components, respectively. An overdot denotes derivative with respect to *t*. The other dimensionless parameters are defined as:

$$f_1(t) = T_1(t)/(\omega_c^2 I_1), \; f_N(t) = T_{N+1}(t)/(\omega_c^2 I_{N+1}), \quad (6a,b)$$

$$g_n(t) = \begin{cases} \bar{g}_n(t), & n = odd, \\ \bar{g}_n(t)/b_c, & n = even, \end{cases} \quad (6c)$$

$$\omega_{n(n-1)}^2 = \begin{cases} \dfrac{r_n\bar{k}_{n-1}b_c}{I_n\omega_c^2}, & n = odd, \\ \dfrac{r_n\bar{k}_{n-1}}{I_n\omega_c^2 b_c}, & n = even, \end{cases}$$

$$\omega_{nn}^2 = \begin{cases} \left(\dfrac{1}{I_n} + \dfrac{1}{I_{n+1}}\right)\dfrac{\bar{k}_n}{\omega_c^2}, & n = odd, \\ \left(\dfrac{r_n^2}{I_n} + \dfrac{r_{n+1}^2}{I_{n+1}}\right)\dfrac{\bar{k}_n}{\omega_c^2}, & n = even, \end{cases} \quad (6d,e)$$

$$\omega_{n(n+1)}^2 = \begin{cases} \dfrac{r_{n+1}\bar{k}_{n+1}b_c}{I_{n+1}\omega_c^2}, & n = odd, \\ \dfrac{r_{n+1}\bar{k}_{n+1}}{I_{n+1}\omega_c^2 b_c}, & n = even, \end{cases}$$

$$\zeta_{n(n-1)} = \begin{cases} \dfrac{r_n c_{n-1} b_c}{2 I_n \omega_{n(n-1)} \omega_c}, & n = odd, \\ \dfrac{r_n c_{n-1}}{2 I_n \omega_{n(n-1)} \omega_c b_c}, & n = even, \end{cases} \qquad (6f,g)$$

$$\zeta_{nn} = \begin{cases} \frac{1}{2}\left(\dfrac{1}{I_n} + \dfrac{1}{I_{n+1}}\right) \dfrac{c_n}{\omega_{nn} \omega_c}, & n = odd, \\ \frac{1}{2}\left(\dfrac{r_n^2}{I_n} + \dfrac{r_{n+1}^2}{I_{n+1}}\right) \dfrac{c_n}{\omega_{nn} \omega_c}, & n = even, \end{cases}$$

$$\zeta_{n(n+1)} = \begin{cases} \dfrac{r_{n+1} c_{n+1} b_c}{2 I_{n+1} \omega_c \omega_{n(n+1)}}, & n = odd, \\ \dfrac{r_{n+1} c_{n+1}}{2 I_{n+1} \omega_c \omega_{n(n+1)} b_c}, & n = even. \end{cases} \qquad (6h,i)$$

3. Multi-term Harmonic Balance Solution

The multi-term Harmonic Balance method is based on the assumption that the external excitations $f_n(t)$ and $e_n(t)$, time-varying coefficients $\kappa_n(t)$, the steady-state solutions $p_n(t)$ and nonlinear functions $g_n(t)$ are all periodic. These functions are given in Fourier series form as:

$$\kappa_n(t) = 1 + \sum_{h=1}^{K} [\kappa_{2h}^{(n)} \cos(h m_n \Lambda t) + \kappa_{2h+1}^{(n)} \sin(h m_n \Lambda t)], \quad n = even, \qquad (7a)$$

$$e_n(t) = E_1^{(n)} + \sum_{r=1}^{\Gamma} [E_{2r}^{(n)} \cos(r m_n \Lambda t) + E_{2r+1}^{(n)} \sin(r m_n \Lambda t), \quad n = even, \qquad (7b)$$

$$f_n(t) = f_1^{(n)} + \sum_{\ell=1}^{L} [f_{2\ell}^{(n)} \cos(\ell \Lambda t) + f_{2\ell+1}^{(n)} \sin(\ell \Lambda t)], \quad n = 1, 2 \ldots, N, \qquad (7c)$$

$$p_n = u_1^{(n)} + \sum_{r=1}^{R} [u_{2r}^{(n)} \cos(\frac{r \Lambda t}{\eta}) + u_{2r+1}^{(n)} \sin(\frac{r \Lambda t}{\eta}), \qquad n = 1, 2, \ldots, N \qquad (7d)$$

$$g_n = v_1^{(n)} + \sum_{r=1}^{R} [v_{2r}^{(n)} \cos(\frac{r \Lambda t}{\eta}) + v_{2r+1}^{(n)} \sin(\frac{r \Lambda t}{\eta}), \quad n = even \qquad (7e)$$

Here, $\Lambda = Z\Omega / \omega_c$ is the fundamental dimensionless frequency of the stiffness (tooth pass frequency) of a chosen gear mesh, where Z and Ω are the number of teeth and rotational frequency of one of the gears forming the mesh, and the integer multipliers m_n ($n = even$) are defined to include commensurate stiffness frequency ratios of the various gear meshes. In equation (7d), $\mathbf{u} = [u_1^{(1)} \; u_{2r}^{(1)} \; u_{2r+1}^{(1)} \; \cdots, u_1^{(n)}, \; u_{2r}^{(n)}, \; u_{2r+1}^{(n)} \; \cdots \; u_1^{(N)} \; u_{2r}^{(N)} \; u_{2r+1}^{(N)}]^T$ are unknown coefficients of the assumed solution, and η is the sub-harmonic index required to find sub-harmonic motions. Defining $\theta = \Lambda t / \eta$, substituting equations (7) into equation (6), and enforcing harmonic balance, the following set of $N(2R+1)$ non-linear coupled nonlinear algebraic equations are obtained:

$$\mathbf{S}(\mathbf{u}, \mathbf{v}, \Lambda) = \mathbf{0} \qquad (8)$$

where vectors **u**, **v** and **S** have dimension $N(2R+1)$. For $n = odd$, the elements of **S** vector are given as ($r \in [1, R]$)

$$S_1^{(n)} = \omega_{n(n-1)}^2 [v_1^{(n-1)} + \tfrac{1}{2} \sum_{h=1}^{H} \varphi_h^{(n-1)}] + \omega_{nn}^2 u_1^{(n)} - \omega_{n(n+1)}^2 [v_1^{(n+1)} + \frac{1}{2} \sum_{h=1}^{H} \varphi_h^{(n+1)}] - f_1^{(n)}, \qquad (9a)$$

$$\begin{aligned} S_{2r}^{(n)} = & -(\frac{r\Lambda}{\eta})^2 u_{2r}^{(n)} + 2\zeta_{n(n-1)} \omega_{n(n-1)} \frac{r\Lambda}{\eta} u_{2r+1}^{(n-1)} \\ & + 2\zeta_{nn} \omega_{nn} \frac{r\Lambda}{\eta} u_{2r+1}^{(n)} - 2\zeta_{n(n+1)} \omega_{(n)(n+1)} \frac{r\Lambda}{\eta} u_{2r+1}^{(n+1)} \\ & + \omega_{nn}^2 u_{2r}^{(n)} - f_{2r/\eta}^{(n)} + \omega_{n(n-1)}^2 [\Phi_{2r}^{(n-1)} \\ & + \frac{1}{2} \sum_{h=1}^{H} (\kappa_{2h}^{(n-1)} \psi 2_{rh}^{(n-1)} + \kappa_{2h+1}^{(n-1)} \psi 1_{rh}^{(n-1)})] \\ & - \omega_{n(n+1)}^2 [\Phi_{2r}^{(n+1)} + \frac{1}{2} \sum_{h=1}^{H} (\kappa_{2h}^{(n+1)} \psi 2_{rh}^{(n+1)} + \kappa_{2h+1}^{(n+1)} \psi 1_{rh}^{(n+1)})], \end{aligned} \qquad (9b)$$

$$\begin{aligned} S_{2r+1}^{(n)} = & -(\frac{r\Lambda}{\eta})^2 u_{2r+1}^{(n)} - 2\zeta_{n(n-1)} \omega_{n(n-1)} \frac{r\Lambda}{\eta} u_{2r}^{(n-1)} \\ & - 2\zeta_{nn} \omega_{nn} \frac{r\Lambda}{\eta} u_{2r}^{(n)} + 2\zeta_{n(n+1)} \omega_{(n)(n+1)} \frac{r\Lambda}{\eta} u_{2r}^{(n+1)} \\ & + \omega_{nn}^2 u_{2r+1}^{(n)} - f_{2r+1}^{(n)} \\ & + \omega_{n(n-1)}^2 [\Phi_{2r+1}^{(n-1)} + \frac{1}{2} \sum_{h=1}^{H} ((\kappa_{2h}^{(n-1)} \psi 3_{rh}^{(n-1)} + \kappa_{2h+1}^{(n-1)} \psi 4_{rh}^{(n-1)})] \\ & - \omega_{n(n+1)}^2 [\Phi_{2r+1}^{(n+1)} + \frac{1}{2} \sum_{h=1}^{H} ((\kappa_{2h}^{(n+1)} \psi 3_{rh}^{(n+1)} + \kappa_{2h+1}^{(n+1)} \psi 4_{rh}^{(n+1)})]. \end{aligned} \qquad (9c)$$

For $n = even$, the elements of **S** are given as ($r \in [1, R]$)

$$S_1^{(n)} = -\omega_{n(n-1)}^2 u_1^{(n-1)} + \omega_{n(n+1)}^2 u_1^{(n+1)} + \omega_{nn}^2 [v_1^{(n)} + \frac{1}{2} \sum_{h=1}^{H} \varphi_h^{(n)}], \qquad (9d)$$

$$\begin{aligned} S_{2r}^{(n)} = & -(\frac{r\Lambda}{\eta})^2 u_{2r}^{(n)} + (\frac{r\Lambda}{\eta})^2 E_{2(r/m_n \eta)}^{(n)} - 2\zeta_{n(n-1)} \omega_{n(n-1)} \frac{r\Lambda}{\eta} u_{2r+1}^{(n-1)} \\ & + 2\zeta_{nn} \omega_{nn} \frac{r\Lambda}{\eta} u_{2r+1}^{(n)} + 2\zeta_{n(n+1)} \omega_{n(n+1)} \frac{r\Lambda}{\eta} u_{2r+1}^{(n+1)} - \omega_{n(n-1)}^2 u_{2r}^{(n-1)} \\ & + \omega_{n(n+1)}^2 u_{2r}^{(n+1)} + \omega_{nn}^2 [\Phi_{2r}^{(n)} + \frac{1}{2} \sum_{h=1}^{H} (\kappa_{2h}^{(n)} \psi 2_{rh}^{(n)} + \kappa_{2h+1}^{(n)} \psi 1_{rh}^{(n)})], \end{aligned} \qquad (9e)$$

$$\begin{aligned} S_{2r+1}^{(n)} = & -(\frac{r\Lambda}{\eta})^2 u_{2r+1}^{(n)} + (\frac{r\Lambda}{\eta})^2 E_{2(r/m_n \eta)+1}^{(n)} + 2\zeta_{n(n-1)} \omega_{n(n-1)} \frac{r\Lambda}{\eta} u_{2r}^{(n-1)} \\ & - 2\zeta_{nn} \omega_{nn} \frac{r\Lambda}{\eta} u_{2r}^{(n)} - 2\zeta_{n(n+1)} \omega_{n(n+1)} \frac{r\Lambda}{\eta} u_{2r}^{(n+1)} - \omega_{n(n-1)}^2 u_{2r+1}^{(n-1)} \\ & + \omega_{n(n+1)}^2 u_{2r+1}^{(n+1)} + \omega_{nn}^2 [\Phi_{2r+1}^{(n)} + \frac{1}{2} \sum_{h=1}^{H} (\kappa_{2h}^{(n)} \psi 3_{rh}^{(n)} + \kappa_{2h+1}^{(n)} \psi 4_{rh}^{(n)})]. \end{aligned} \qquad (9f)$$

In equations for $S_i^{(1)}$ and $S_i^{(N)}$, $i \in (1, 2R+1)$, the terms having indices less than one or larger than N, respectively, must be omitted. In addition, parameters ψi, φ and Φ in equations (9) are defined below

$$\psi 1_{rh}^{(n)} = v_{2(h\eta m_n - r)+1}^{(n)} + v_{2(h\eta m_n + r)+1}^{(n)} - v_{2(r-h\eta m_n)+1}^{(n)}, \quad (10a)$$

$$\psi 2_{rh}^{(n)} = v_{2(h\eta m_n - r)}^{(n)} + v_{2(h\eta m_n + r)}^{(n)} + v_{2(r-h\eta m_n)}^{(n)}, \quad (10b)$$

$$\psi 3_{rh}^{(n)} = -v_{2(h\eta m_n - r)+1}^{(n)} + v_{2(h\eta m_n + r)+1}^{(n)} + v_{2(r-h\eta m_n)+1}^{(n)}, \quad (10c)$$

$$\psi 4_{rh}^{(n)} = v_{2(h\eta m_n - r)}^{(n)} - v_{2(h\eta m_n + r)}^{(n)} + v_{2(r-h\eta m_n)}^{(n)}, \quad (10d)$$

$$\varphi_h^{(n)} = \kappa_{2(h/\eta m_n)}^{(n)} v_{2h}^{(n)} + \kappa_{2(h/\eta m_n)+1}^{(n)} v_{2h+1}^{(n)}, \quad (10e)$$

$$\Phi_{2r}^{(n)} = v_{2r}^{(n)} + v_1^{(n)} \kappa_{2(r/\eta m_n)}^{(n)},$$

$$\Phi_{2r+1}^{(n)} = v_{2r+1}^{(n)} + v_1^{(n)} \kappa_{2(r/\eta m_n)+1}^{(n)} \quad (10f,g)$$

In later steps, the selection of Λ as a control parameter to solve for the elements of $\mathbf{u}$ using Newton-Raphson iteration method poses difficulties The determinant of the Jacobian matrix also approaches zero near the bifurcation points. This can be avoided by switching to another unknown as the control parameter, leaving the dimensionless frequency Λ and the other elements of the solution vector $\mathbf{u}$ as unknowns to be determined. In order to implement this, $\mathbf{u}$ is expanded to $\mathbf{U} = [\mathbf{u}^T, u_{2R+2)}^{(N)}]^T$ where $u_{2R+2)}^{(N)} = \Lambda$. Accordingly, the following dummy equation is added to equation (9)

$$S_{2R+2}^{(N)} = u_j^{(i)} - u^* \quad (11)$$

where $u_j^{(i)} = u_{2R+2)}^{(N)} = \Lambda$ or the values of the indices $j \in [1, 2R+1]$ and $i \in [1, N]$ define which element is chosen as a control parameter, and u^* is a numerical value prescribed to the control parameter .

The coefficients of the nonlinear displacement functions $v_i^{(n)}$ are represented in terms of $u_i^{(n)}$ and $u_{2R+2}^{(N)}$ ($n \in [1, N]$, $i \in [1, 2R+1]$) by using Discrete Fourier transforms. The values of the $p_n(t)$ and $g_n(t)$ at the discrete time $t = q\rho$ ($q \in [0, Q-1]$) are given as

$$p_{nq} = u_1^{(n)} + \sum_{r=1}^{R} [u_{2r}^{(n)} \cos(\frac{2\pi rq}{Q}) + u_{2r+1}^{(n)} \sin(\frac{2\pi rq}{Q})], \quad (12a)$$

$$g_{nq} = \begin{cases} p_{nq}(t) - b_n, & p_{nq}(t) > b_n \\ 0, & |p_{nq}(t)| \le b_n \\ p_{nq}(t) + b_n, & p_{nq}(t) < -b_n \end{cases} \quad n = even. \quad (12b)$$

Here, $\rho = (2\pi\eta / Q\Lambda)$ where Q is the total number of the discrete points. The coefficients of $g_n(t)$ are determined by using the inverse Fourier transforms such that ($r \in [1, R]$)

$$v_1^{(n)} = \frac{1}{Q} \sum_{q=0}^{Q-1} g_{nq},$$

$$v_{2r}^{(n)} = \frac{2}{Q} \sum_{q=0}^{Q-1} g_{nq} \cos(\frac{2\pi rq}{Q}),$$

$$v_{2r+1}^{(n)} = \frac{2}{Q} \sum_{q=0}^{Q-1} g_{nq} \sin(\frac{2\pi rq}{Q}) \quad (13a\text{-}c)$$

These $v_i^{(n)}$ values and the Newton-Raphson recurrence formula

$$\mathbf{U}^{(m)} = \mathbf{U}^{(m-1)} - [\mathbf{J}^{-1}]^{(m-1)} \mathbf{S}^{(m-1)} \quad (14)$$

are used to solve equations (9) for $\mathbf{U}$, where $\mathbf{U}^{(m-1)}$ and $\mathbf{U}^{(m)}$ are the previous and the current iteration values of the vector $\mathbf{U}$, respectively, and $[\mathbf{J}^{-1}]^{(m-1)}$ is the inverse of the Jacobian matrix of the vector $\mathbf{S}$ estimated at the previous point $(m-1)$. Elements of the Jacobian matrix $\mathbf{J}$ for this model are defined in Appendix A. The Floquet theory is used to determine the stability of the steady-state motions as describe in reference [19].

4. Results

A three-shaft gear train (6-DOF semi-definite model) is considered as the example system. It consists of two gear pairs of identical dimensionless parameters connected to each other and to the prime mover and load inertias via torsionally flexible shafts. The dimensionless parameters are calculated by using equations (6) and the dimensional parameters listed in Table 1.

Table 1. Dimensional parameters of the example gear pair

Parameter	Gear 1	Gear 2	Gear 3	Gear 4
Base circle radius, m	0.05	0.10	0.05	0.10
Mass, kg	1.85	7.4	3.7	14.81
Inertia, kg – m^2	0.0023	0.037	0.0046	0.074
Average mesh stiffness, N/m	$2.5(10)^8$		$5(10)^8$	
Mesh damping coefficient, N-s/m	1360		2720	
Torsional stiffness of the input and output shafts, N-m/rad	$1.0(10)^3$			
Shaft damping ratios	0.01			
Input inertia, kg – m^2	$2.30(10)^{-7}$			
Output inertia, kg – m^2	$2.30(10)^{-7}$			

In order to limit the size of the parameter study, mostly harmonic mesh stiffness functions with amplitude $\kappa_2^{(2)} = \kappa_4^{(2)} = 0.3$ are considered ($K = 1$ in equation (7)).

This corresponds to a spur gear pair with an involute contact ratio value of 1.7. A constant external input torque of $T_1 = 150$ *N-m* ($L = 0$ in equation (7)) corresponding to $f_1(t) = f_1^{(1)} = 11{,}000$ and $f_5(t) = f_1^{(5)} = 4 f_1^{(1)}$ is considered. All gears are assumed to be free of profile errors so that all $e_i(t) = 0$. A characteristic length of $\bar{b}_c = 30\,\mu m$ is considered that represents half magnitude of the gear backlash so that $b_1 = b_2 = 1.0$. A characteristic frequency $\omega_c = 9{,}870$ rad/s is used. In addition, the fundamental mesh frequencies of both gear pairs are considered equal ($m_2 = m_4 = 1$) unless specified. The values of the mesh damping coefficients $\bar{c}_i$ ($i = 2, 4$) in Table 1 are such that

they correspond to a damping ratio of ζ_m=0.05, given $c_i = 2\zeta_m\sqrt{k_{i,m}m_{i,i+1}}$ where $m_{i,i+1} = I_i I_{i+1}/(r_i^2 I_{i+1} + r_{i+1}^2 I_i)$. Similarly, the values of shaft damping coefficient $\bar{c}_i$ ($i = 1,3,5$) correspond to a shaft damping ratio of ζ_s=0.01.

The results in the following sections will be presented in the form of $p_2^{(rms)}$ and $p_4^{(rms)}$ versus the dimensionless frequency Λ. Here $p_i^{(rms)}$ is the root-mean-square (rms) amplitude to $p_i(t)$ defined as $p_i^{(rms)} = \{\sum_{r=1}^{R}[A_r^{(i)}]^2\}^{1/2}$ where $A_r^{(i)} = \{[u_{2r}^{(i)}]^2 + [u_{2r+1}^{(i)}]^2\}^{1/2}$ is the r-th harmonic amplitude. $p_2^{(rms)}$ and $p_4^{(rms)}$ are of primary interest here since these parameters represent gear mesh displacements that are directly proportional to dynamic gear mesh forces.

4.1. Multi-term Harmonic Balance versus Numerical Integration

Figure 3 shows period-1 ($\eta = 1$ in equation (7)) HBM solution $p_2^{(rms)}$ and $p_4^{(rms)}$ as a function of Λ for a system having $\kappa_2^{(2)} = \kappa_2^{(4)} = 0.3$, $f_1^{(1)} = 11000$, and $k_3 = 1.0(10)^8$ N-m/rad. The thick and thin solid lines denote the stable and unstable harmonic balance motions for $R = 6$. Figure 3 also shows the stable and unstable HBM solutions for the corresponding linear time-varying system ($b_1 = b_2 = 0$) as thick and thin dashed lines, respectively. In addition, the direct numerical integration results for both nonlinear and linear systems are represented by square symbols. As shown in Figure 3, the 6-term HBM solutions match well with the numerical integration solutions for both the nonlinear and linear cases. The range of Λ includes primary resonances at $\Lambda = \omega_{a,n} = 0.96$ and $\Lambda = \omega_{b,n} = 1.86$ as well as a super-harmonic resonance $\Lambda = \omega_{an}/2 = 0.48$, where $\omega_{a,n}$ and $\omega_{b,n}$ are two of the natural frequencies.

Both the nonlinear and the corresponding linear models result in the same vibration amplitudes at frequencies where tooth contact is maintained all the time and hence, the gear backlash nonlinearity is not a factor. As Λ approaches natural frequencies $\omega_{a,n} = 0.96$ and $\omega_{b,n} = 1.86$, primary resonances with characteristic softening-type nonlinear curves are obtained. This is solely because the teeth loose contact during a portion of the meshing cycle [19,20]. The softening upper branch of the primary resonance at $\omega_{a,n} = 0.96$ also exhibits a hardening type curve sloped to the right. This corresponds to the back collisions (contact at the unloaded tooth flank) in addition to tooth separations, which is more clear for $p_4^{(rms)}$. It is also noted in Figure 3 is that there is a range of Λ in which no stable period-1 motions are found. This corresponds to the parametric resonance at $\Lambda = 2\omega_{a,n}$. As it will be illustrated later, this range is dictated by period-2 sub-harmonic motions.

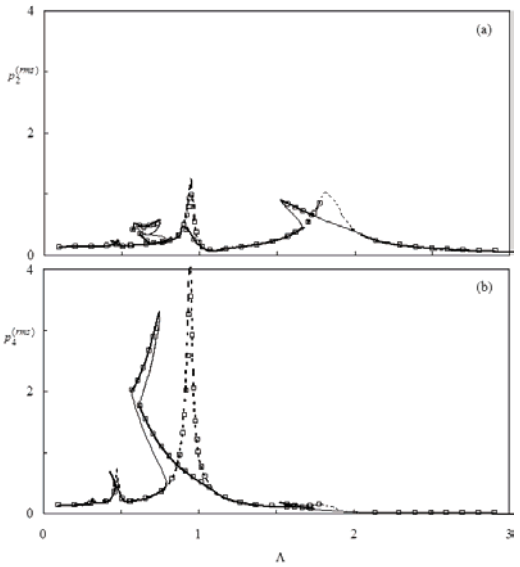

Figure 3: Comparison of period-1 multi-term HBM ($R = 6$) and numerical integration results for $K = 1$, $\kappa_2^{(2)} = \kappa_2^{(4)} = 0.3$, $f_1^{(1)} = 11{,}000$, and $k_3 = 10^8$ N-m/rad. (—) Stable and (——) unstable solutions of the nonlinear model, (- - -) stable and (- - -) unstable solutions of the corresponding linear model, and (□) numerical integration solutions. (a) $p_2^{(rms)}$ and (b) $p_4^{(rms)}$

4.2. Influence of Torsional Shaft Flexibility

In Figure 4, effect of k_3 on period-1 $p_i^{(rms)}$ is illustrated. In order to understand this figure better, the variation of the natural frequencies of the corresponding linear time-invariant system are plotted in Figure 5 against the torsional stiffness k_3 of the shaft connecting the gear pairs to each other.

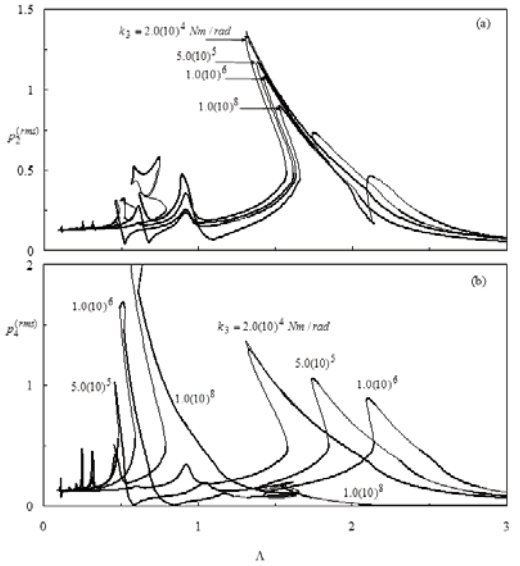

Figure 4: Influence of the shaft stiffness k_3 on period-1 HBM solutions for $K = 1$, $\kappa_2^{(2)} = \kappa_2^{(4)} = 0.3$ and $f_1^{(1)} = 11{,}000$; (a) $p_2^{(rms)}$ and (b) $p_4^{(rms)}$. (—) Stable and (——) unstable HBM solutions

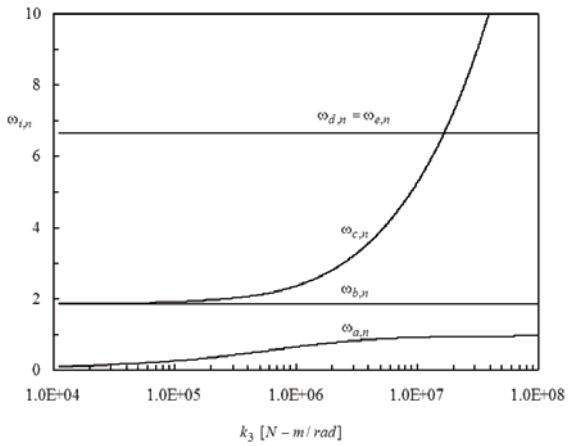

Figure 5: Variation of natural frequencies $\omega_{i,n}$ ($i = a,b,\ldots,e$) of the corresponding linear time-invariant system with k_3

Two of the natural frequencies are $\omega_{d,n} = \omega_{e,n} = 6.65$ regardless of the value of k_3. For the system defined in Table 1, these modes are dominated by the deflections of the shafts connecting the prime mover and load inertias to the respective gears and $\omega_{d,n} \approx \sqrt{k_1 / I_1}/\omega_c$ and $\omega_{e,n} \approx \sqrt{k_5 / I_6}/\omega_c$ where k_1 and k_5 are torsional stiffnesses of these shafts, and I_1 and I_6 are the inertias of the prime mover and the load. For smaller values of k_3, say $k_3 < 10^5$ N-m/rad, the two gear pairs are dynamically uncoupled and each gear pair acts independently as single gear pairs. In this case, $\omega_{a,n} \approx 0$, $\omega_{b,n} \approx \sqrt{\bar{k}_4 / m_{34}}/\omega_c$ and $\omega_{c,n} \approx \sqrt{\bar{k}_2 / m_{12}}/\omega_c$, where m_{12} and m_{34} are equivalent masses of the first and second gear pairs, and $\bar{k}_2$ and $\bar{k}_4$ are the average mesh stiffness values. Since both gear pairs of the example system have the same dimensionless parameters, $\omega_{b,n} \approx \omega_{c,n} \approx 1.86$ for small values of k_3. On the other hand, for $k_3 > 10^8$ N-m/rad, the two gear pairs are connected almost rigidly and $\omega_{a,n} = 0.96$ and $\omega_{b,n} = 1.86$ while $\omega_{c,n}$ is clearly outside that frequency range of interest ($\Lambda \in [0,3]$). Finally, at intermediate shaft stiffness values, say $k_3 = 5(10)^5$, all three natural frequencies $\omega_{a,n}$, $\omega_{b,n}$ and $\omega_{c,n}$ are non-zero and within the frequency range considered. Therefore, resonance peaks should be expected at these frequencies. Figure 4 considers four different k_3 values, $2(10)^4$ N-m/rad (very soft), $5(10)^5$ and 10^6 N-m/rad (intermediate), and 10^8 N-m/rad. (very stiff). When $k_3 = 2(10)^4$ N-m/rad, the two gear pairs are dynamically uncoupled, and since both gear pairs of the example system have identical dimensionless parameters, $p_2^{(rms)} = p_4^{(rms)}$ both having primary resonance peaks at $\omega_{b,n} \approx \omega_{c,n} = 1.86$. On the other hand, a stiffness value of $k_3 = 10^8$ N-m/rad is large enough to provide an almost rigid connection between gears 2 and 3 such that $\theta_3(t) \approx \theta_4(t)$. According to Figure 4, the first gear mesh natural frequency is approximately twice the second natural frequency $\omega_{b,n} \approx 2\omega_{a,n} = 1.86$. As a result, two primary resonances at $\Lambda = \omega_{a,n} = 0.96$ and $\Lambda = \omega_{b,n} = 1.86$ as well as a super-harmonic resonance $\Lambda = \omega_{a,n} / 2 = 0.48$ are evident in Figure 4 when $k_3 = 10^8$ N-m/rad. For the other two values $k_3 = 5(10)^5$ and 10^6 N-m/rad, the primary resonances are observed at $\Lambda \approx \omega_{a,n}$, $\Lambda \approx \omega_{b,n}$ and $\Lambda \approx \omega_{c,n}$. The $p_4^{(rms)}$ resonances are more significant at $\Lambda \approx \omega_{a,n}$ and $\Lambda \approx \omega_{c,n}$ while $p_2^{(rms)}$ exhibits a large softening-type resonance near $\Lambda \approx \omega_{b,n}$. Super-harmonic peaks at one-half of the natural frequencies are also present. In addition, the period-1 solutions are unstable in certain Λ ranges, most of which correspond to the parametric instabilities due the gear mesh stiffness fluctuations.

4.3. Influence of Other System Parameters

Influence of the mean force transmitted by the gear train on the steady state period-1 response is shown in Figure 6. The values of the constant dimensionless forces $f_1^{(5)} = 4 f_1^{(1)}$, where $f_1^{(1)}$ =11,000, 7400 and 3700 correspond to input torque values of $T_1 = 150$, 100 and 50 N-m, respectively. The response curves are in agreement with previous observations on single gear pairs [15,16,17], and three-shaft system results [19,20]. Increasing the constant torque applied does not prevent tooth separations from occurring. Larger $f_1^{(1)}$ and $f_1^{(5)}$ values result in higher amplitudes of $p_2^{(rms)}$ and $p_4^{(rms)}$. The primary resonant peak at $\omega_{a,n} \approx 0.96$ exhibits only a softening type behavior for $f_1^{(1)} = 3{,}700$ while the amplitudes are significantly larger for the other two torque values to initiate back collisions and a hardening type curve following the typical softening behavior.

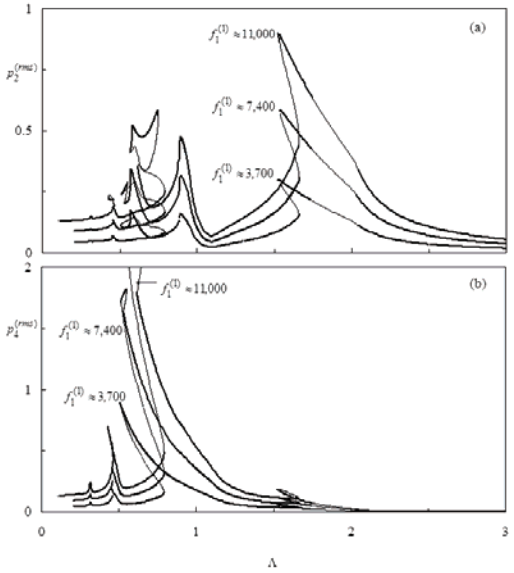

Figure 6: Influence of mean load transmitted on period-1 HBM solutions for $K = 1$, $\kappa_2^{(2)} = \kappa_2^{(4)} = 0.3$ and $k_3 = 10^8$ N-m/rad; (—) Stable and (——) unstable HBM solutions. (a) $p_2^{(rms)}$ and (b) $p_4^{(rms)}$

Likewise, the super-harmonic resonance amplitudes at $\Lambda = \omega_{a,n} / 2 = 0.48$ in Figure 6(b) and at $\Lambda = \omega_{b,n} / 2 = 0.93$ in Figure 6(a) are increased significantly when the torque

is increased. The parametric instability regions near $\Lambda = 2\omega_{a,n}$ and the jump-up frequencies are not influenced by the values of $f_1^{(1)}$ and $f_1^{(5)}$ values. Figure 7 illustrates the influence of the gear mesh stiffness amplitudes on period-1 motions. The mesh stiffness harmonic amplitudes of a spur gear pair depend primarily on the involute contact ratio (a parameter representing the average number of engaged tooth pairs). Four values of harmonic mesh stiffness amplitudes $\kappa_2^{(2)} = \kappa_4^{(2)} = 0.42$, 0.3, 0.2 and 0.1 are considered in Figure 7 corresponding to involute contact ratios of 1.5, 1.7, 1.8 and 1.9, respectively. In this figure, the mesh stiffness amplitudes appear to influence the period-1 response in several ways. (i) Increased $\kappa_2^{(2)} = \kappa_4^{(2)}$ values result in increased response amplitudes as well. This influence is more significant than the one shown in Figure 6 as not only the amplitudes but also the degree of nonlinear behavior is influenced. When $\kappa_2^{(2)} = \kappa_4^{(2)}$ values are low, say 0.1, a minor softening type resonance peak is observed near $\Lambda = \omega_{a,n} = 0.96$ in Figure 7(a) while the primary resonance peak near $\Lambda = \omega_{b,n} = 1.86$ is linear. For $\kappa_2^{(2)} = \kappa_4^{(2)} = 0.2$, both primary resonance peaks become non-linear (tooth separations). For $\kappa_2^{(2)} = \kappa_4^{(2)} \geq 0.3$, back collisions are also initiated near $\Lambda = \omega_{a,n} = 0.96$. (ii) The super-harmonic resonances at $\Lambda = \omega_{a,n}/2 = 0.48$ in Figure 7(b) and at $\Lambda = \omega_{b,n}/2 = 0.93$ in Figure (7a) become significantly larger when $\kappa_2^{(2)} = \kappa_4^{(2)}$ is increased. (iii) Larger $\kappa_2^{(2)} = \kappa_4^{(2)}$ amplitudes are observed to enhance the parametric resonances as well. While there is no unstable region of period-1 motions for $\kappa_2^{(2)} = \kappa_4^{(2)} = 0.1$, a wide band of unstable motions is observed for $\kappa_2^{(2)} = \kappa_4^{(2)} = 0.42$ within $\Lambda \in [1.65, 2.15]$.

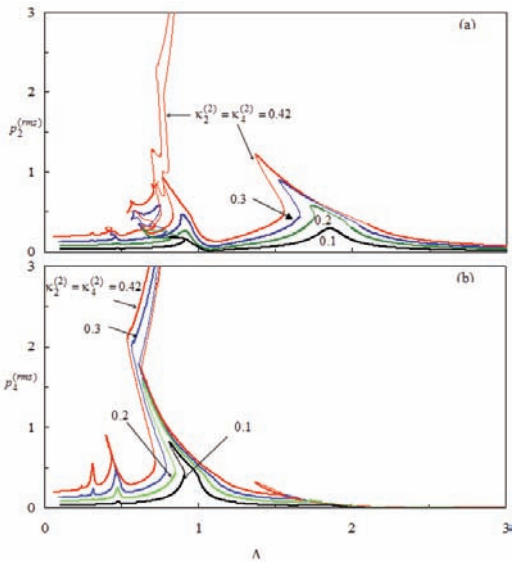

Figure 7: Influence of harmonic mesh stiffness amplitude on period-1 HBM solutions for $k_3 = 10^8$ N-m/rad and $f_1^{(1)} = 11{,}000$; (—) Stable and (——) unstable HBM solutions. (a) $p_2^{(rms)}$ and (b) $p_4^{(rms)}$

Next, higher harmonic amplitudes of the periodic mesh stiffness functions in equation (7a) are also considered to illustrate their influence on the steady-state period-1 motions. In Fig.(8), the five Fourier harmonics of the mesh stiffness functions $\kappa_2(t)$ & $\kappa_4(t)$ are considered to represent an involute contact ratio of 1.5. It was shown in reference [18] that a mesh stiffness function could be approximated to a rectangular waveform which becomes a square wave for an involute contact ratio of 1.5. In this case, even harmonic amplitudes are zero and the first three non-zero harmonics are $\kappa_2^{(2)} = \kappa_2^{(4)} = 0.42$, $\kappa_6^{(2)} = \kappa_6^{(4)} = -0.141$, & $\kappa_{10}^{(2)} = \kappa_{10}^{(4)} = -0.085$ ($K = 5$ in equation (7). In this case, the rms response curves exhibit not only the primary resonances near $\Lambda = \omega_{a,n}$ and $\Lambda = \omega_{b,n}$ and super-harmonic resonance near $\Lambda = \omega_{a,n}/2$ and $\Lambda = \omega_{b,n}/2$ as discussed earlier, but also additional resonance peaks at $\Lambda = \frac{1}{3}\omega_{a,n}$, $\frac{1}{3}\omega_{b,n}$, $\frac{1}{5}\omega_{a,n}$ and $\frac{1}{5}\omega_{b,n}$ due to the higher harmonic terms of the mesh stiffness ($\kappa_6^{(2)} = \kappa_6^{(4)} = -0.141$ and $\kappa_{10}^{(2)} = \kappa_{10}^{(4)} = -0.085$).

Influence of gear mesh damping ratio ζ_m is investigated next in Figure.9. The steady-state period-1 solutions are shown for $\zeta_m = 0.05$, 0.03 and 0.01. The value of the gear mesh damping is observed to affect the response amplitudes, level of nonlinear[19] behavior exhibited and the width of parametric instability frequency bands. The system with low damping values demonstrates larger amplitudes, dominant primary & super-harmonic resonances as well as wider frequency ranges of instability.

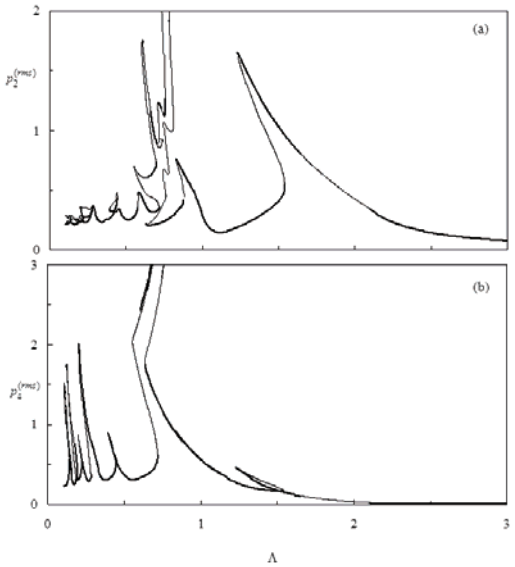

Figure 8: Period-1 HBM solutions for periodic ($K=5$) mesh stiffness amplitudes $\kappa_2^{(2)}=\kappa_2^{(4)}=0.42$, $\kappa_6^{(2)}=\kappa_6^{(4)}=-0.141$, and $\kappa_{10}^{(2)}=\kappa_{10}^{(4)}=-0.085$ for $f_1^{(1)}=11{,}000$ and $k_3=10^8$ N-m/rad; (—) Stable and (——) unstable HBM solutions. (a) $p_2^{(rms)}$ and (b) $p_4^{(rms)}$

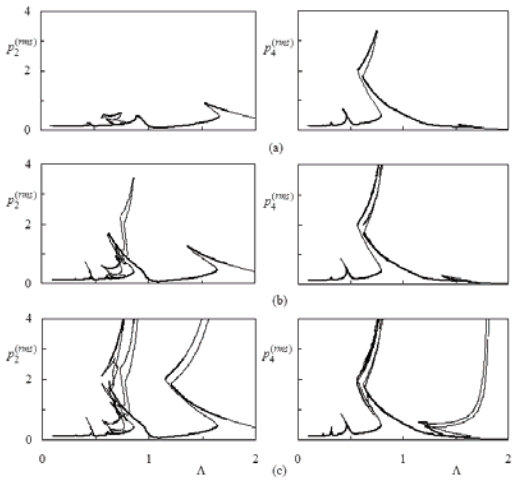

Figure 9: Influence of mesh damping ratio ζ_m on period-1 HBM solutions for $k_3=10^8$ N-m/rad and $f_1^{(1)}=11{,}000$; (—) Stable and (——) unstable HBM solutions. (a) $\zeta_m=0.05$ (b) $\zeta_m=0.03$ and (c) $\zeta_m=0.01$

The dimensionless mesh (tooth pass) frequency was defined in equation 7(a) as $m_i\Lambda$, where m_i is a multiplier introduced to handle the cases when the mesh frequencies of individual gear pairs are not equal. The results shown up to this point considered $m_2=m_4=1$ indicating that the gear mesh frequencies of both gear pairs are identical. This implies gears 2 and 3 that are connected by the shaft of stiffness k_3 have the same number of teeth, but different modules. In general, however, this may not be the case. Two different situations are illustrated in Figures 10 and 11 to demonstrate the changes in steady state response when $m_2\neq m_4$.

In Figure.10, the response is shown for the case when $m_2=1$ and $m_4=2$ where the primary resonances are near the frequencies $\Lambda\approx\omega_{a,n}/m_2=0.96$, $\Lambda\approx\omega_{a,n}/m_4=0.48$, $\Lambda\approx\omega_{b,n}/m_2=1.86$ and $\Lambda\approx\omega_{b,n}/m_4=0.93$. As two of the primary resonance frequencies coincide, $\omega_{a,n}/m_2\approx\omega_{b,n}/m_4$, the period-1 response curves near this frequency include several jump discontinuities. In addition, back collisions are evident at the first two resonance frequencies. As the second example, consider a system having $m_2=3$ and $m_4=2$ whose response is shown in Figure 11. In this case, the primary resonance frequencies are at $\Lambda\approx\omega_{a,n}/m_2=0.32$, $\Lambda\approx\omega_{a,n}/m_4=0.48$, $\Lambda\approx\omega_{b,n}/m_2=0.65$ and $\Lambda\approx\omega_{b,n}/m_4=0.98$. Since these four resonance peaks are spaced closely within narrow frequency range, the response curves become rather complex with several bifurcations and stable and unstable regions.

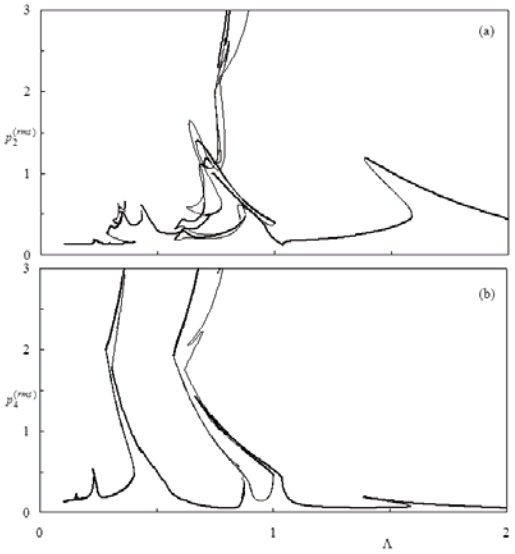

Figure 10: Period-1 HBM solutions due harmonic ($K=1$) mesh stiffness amplitudes $\kappa_2^{(2)}=\kappa_2^{(4)}=0.3$ for $m_2=1$, $m_4=2$, $f_1^{(1)}=11{,}000$ and $k_3=10^8$ N-m/rad; (—) stable and (——) unstable HBM solutions. (a) $p_2^{(rms)}$ and (b) $p_4^{(rms)}$

4.4. Sub-harmonic Resonances and Period-n Motions

Several of the forced response curves shown earlier included regions of unstable period-1 motions at the parametric resonance frequency, $\Lambda\approx 2\omega_{a,n}=1.92$. Although it was not shown in these figures, the same is true for $\Lambda\approx 2\omega_{b,n}=3.92$ as well. In reference [20], period-1 motions were shown to lose their stability at the boundaries of these regions of instability to yield stable period-2 motions. In Figure.12, stable and unstable period-2 motions are shown near $\Lambda\approx 2\omega_{a,n}$ and $\Lambda\approx 2\omega_{b,n}$. These motions are obtained by setting $\eta=2$ in equation (7d,e) and (9).

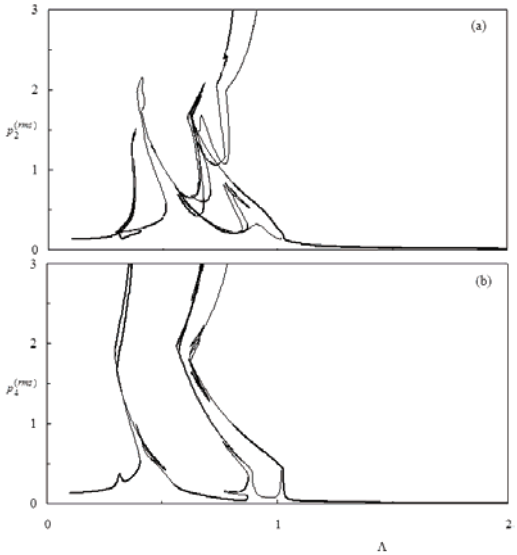

Figure 11: Period-1 HBM solutions due to harmonic ($K=1$) mesh stiffness amplitudes $\kappa_2^{(2)}=\kappa_2^{(4)}=0.3$ for $m_2=3$, $m_4=2$, $f_1^{(1)}=11{,}000$ and $k_3=10^8$ N-m/rad; (—) stable and (——) unstable HBM solutions. (a) $p_2^{(rms)}$ and (b) $p_4^{(rms)}$

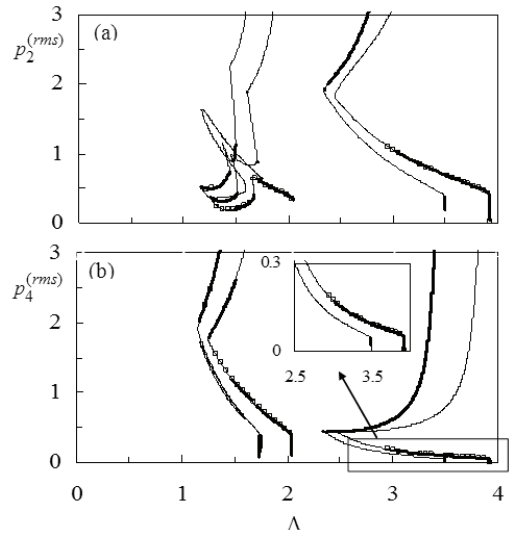

Figure 12: NI and Period-2 sub-harmonic HBM solutions due to harmonic ($K=1$) mesh stiffness amplitudes $\kappa_2^{(2)}=\kappa_2^{(4)}=0.3$ for $f_1^{(1)}=11{,}000$ and $k_3=10^8$ N-m/rad; (—) stable and (——) unstable HBM solutions, (∑) NI solution. (a) $p_2^{(rms)}$ and (b) $p_4^{(rms)}$

The amplitudes of the motions are very large such that back collisions are also obtained in the form of period-2 motions. As these stable period-2 motions cover the entire ranges of unstable perod-1 motions, any catastrophic increases of amplitudes in these ranges are prevented solely due to the gear backlash nonlinearity. Similarly, in Figure.13, period-3 sub-harmonic motions are found to exist near the parametric resonance frequency $\Lambda \approx 3\omega_{a,n}$ by setting $\eta=3$. These motions coexist with stable period-1 motions. However, they form isolated islands which are not connected to the period-1 motions, suggesting that the system may not exhibit such motions unless disturbed drastically.

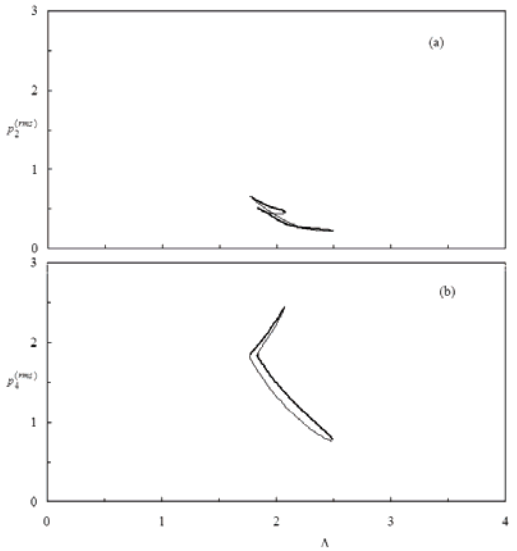

Figure 13: Period-3 sub-harmonic HBM solutions due to harmonic ($K=1$) mesh stiffness amplitudes $\kappa_2^{(2)}=\kappa_2^{(4)}=0.3$ for $f_1^{(1)}=11{,}000$ and $k_3=10^8$ N-m/rad; (—) stable and (——) unstable HBM solutions. (a) $p_2^{(rms)}$ and (b) $p_4^{(rms)}$

5. Conclusions

A non-linear time-varying torsional dynamic model of multi-mesh gear train formed by *M* shafts coupled to each other by $M-1$ gear pairs. The dynamic model included the gear backlash nonlinearity allowing tooth separations and back collisions, the gear mesh stiffness fluctuations, and torsional flexibilities of the shafts. A multi-term Harmonic Balance formulation in conjunction with discrete Fourier Transforms and a Parametric Continuation technique were proposed to obtain the period-n, steady-state motions. The accuracy of solution method was demonstrated through a comparison to the direct numerical integration results.

A three-shaft, two gear-pair example gear train was used to study the influence of the key system parameters. The torsional stiffness of the shaft connecting the gear pairs was shown to influence not only modal characteristics of the system, but also the nonlinear response. It was also shown that the gear mesh stiffness amplitude, gear mesh damping ratio, the torque transmitted and the ratio of the gear mesh frequencies all influenced the forced response significantly. In addition to primary and super-harmonic resonances of period-1 motions, the sub-harmonic resonances of period-2 and period-3 motions were also shown to exist foe the example system considered.

Acknowledgements

The authors thank Hashemite University, Jordon, for supporting the authors during this study.

References

[1] H. Vinayak, R. Singh, and C. Padmanabhan, Linear dynamic analysis of multi-mesh transmissions containing external rigid gears, Journal of Sound and Vibration, Vol.185 ,1995, 1-32.

[2] S. H. Choi, J. Glienicke, D. C. Han, and K. Urlichs, Dynamic gear load due to coupled lateral, torsional and axial vibrations in a helical geared system, Journal of Vibration and Acoustics, Vol. 121, 1999, 141-148.

[3] T. C. Lim, and J. Li, Dynamic analysis of multi-mesh counter-shaft transmission, Journal of Sound and Vibrations, Vol.219, 1999, 905-918.

[4] A. Kahraman, Dynamic analysis of a multi-mesh helical gear train, Journal of Mechanical Design, Vol.116,1994, 706-712.

[5] H. Iida, A. Tamura, K. Kikuchi, and H. Agata, Coupled torsional-flexural vibration of a shaft in a geared system of rotors (1st report), Bulletin of the JSME, Vol.23, 1980, 2111-2117.

[6] H. Iida, A. Tamura, and M. Oonishi, Coupled torsional-flexural vibration of a shaft in a geared system (3rd report), Bulletin of the JSME, Vol.28,1985, 2694-2698.

[7] H. Iida, A. Tamura, and H. Yamamoto, Dynamic characteristics of a gear train system with softly supported shafts, Bulletin of the JSME, Vol.29 ,1986),1811-1816.

[8] T. Iwatsubo, S. Arii, and R. Kawai, Coupled lateral-torsional vibration of rotor system trained by gears, Bulletin of the JSME, Vol.27,1984, 271-277.

[9] K. Umezawa, T. Ajima, and H. Houjoh, Vibration of three axis gear system. Bulletin of JSME, Vol.29,1986, 950-957.

[10] M. Kubur, A. Kahraman, D. Zini, and K. Kienzle, Dynamic analysis of multi-mesh helical gear sets by finite elements, in press, Journal of Vibration and Acoustics, 2004.

[11] M. Benton, M. and A. Seireg, Simulation of responses and instability conditions in a pinion-gear system, Journal of Mechanical Design, Vol.100,1978, 26-32.

[12] M. Benton and A. Seireg, Factors influencing instability and resonances in geared systems, Journal of Mechanical Design, Vol.103,1981, 372-378.

[13] W. Mollers, Parametererregte Schwingungen in einstufigen Zylinderradgetrieben, Ph.D. Dissertation, Rheinisch-Westfalischen Technischen Hochschule Aachen, 1982.

[14] T. Nakada and M. Utagawa, The dynamic loads on gears caused by the varying elasticity of the mating teeth, Proc. of the 6th Japan National Congress for Applied Mechanics,1956, 493-497.

[15] A. Kahraman and G. W. Blankenship, Experiments on nonlinear dynamic behavior of an oscillator with clearance and periodically time-varying parameters, Journal of Applied Mechanics, Vol.64,1997, 217-226.

[16] G. W. Blankenship and A. Kahraman, Steady state forced response of a mechanical oscillator with combined parametric excitation and clearance type non-linearity, Journal of Sound and Vibration, Vol.185, 1994, 734-765.

[17] A. Kahraman, and G. W. Blankenship, Interactions between commensurate parametric and forcing excitations in a system with clearance, Journal of Sound and Vibration, Vol.194, 1996, 317-335.

[18] A. Kahraman and G. W. Blankenship, Effect of involute contact ratio on spur gear dynamics, Journal of Mechanical Design, Vol.121,1999, 112-118.

[19] A. Al-shyyab, and A. Kahraman, Non Non-Linear Dynamic Analysis of a Multi-Mesh Gear Train using Multi-term Harmonic Balance Method: Period-one Motions, in press, Journal of Sound and Vibration,2004.

[20] A. Al-shyyab, and A. Kahraman, Non-linear dynamic analysis of a multi-mesh gear train using multi-term harmonic balance method: sub-harmonic motions, in press, Journal of Sound and Vibration,2004.